catalysts

MDPI

Article

Co-Supported CeO_2Nanoparticles for CO Catalytic Oxidation: Effects of Different Synthesis Methods on Catalytic Performance

Chao Sui *, LeHong Xing, Xue Cai, Yang Wang, Qi Zhou and Minghao Li

College of Chemistry and Chemical Engineering, Mudanjiang Normal University, Mudanjiang 157000, China; xinglehonghit@126.com (L.X.); xuecai@mail.sdu.edu.cn (X.C.); wy1355500@163.com (Y.W.); Zhouqi97823@163.com (Q.Z.); liminghao0624@163.com (M.L.)

* Correspondence: suichao071@163.com; Tel.: +86-0453-8611816

Received: 5 February 2020; Accepted: 16 February 2020; Published: 18 February 2020

Abstract: Hydrothermal and co-precipitation methods were studied as two different methods for the synthesis of CeO_2nanocatalysts. Co/CeO_2 catalysts supported by 2, 4, 6, or 8wt% Co were further synthesized through impregnation and the performance of the catalytic oxidation of CO has been investigated. The highest specific surface area and the best catalytic performance was obtained by the catalyst 4wt% Co/CeO_2 with the CeO_2 support synthesized by the hydrothermal method (4% Co/CeO_2-h), which yielded 100% CO conversion at 130 °C. The formation of CeO_2 nanoparticles was confirmed by TEM analysis. XRD and SEM-EDX mapping analyses indicated that CoO_x is highly dispersed on the 4% Co/CeO_2-h catalyst surface. H_2-TPR and O_2-TPD results showed that 4% Co/CeO_2-h possesses the best redox properties and the highest amount of chemically adsorbed oxygen on its surface among all tested catalysts. Raman and XPS spectra showed strong interactions between highly dispersed Co^{2+} active sites and exposed Ce^{3+} on the surface of the CeO_2 support, resulting in the formation of the strong redox cycle $Ce^{4+} + Co^{2+} \leftrightarrow Ce^{3+} + Co^{3+}$.This may explain that 4% Co/CeO_2-h exhibited the best catalytic activity among all tested catalysts.

Keywords: CO oxidation; Co/CeO_2catalyst; different synthesis methods; redox cycle

1. Introduction

In the last decades, the application of metal oxide nanoparticles in the field of catalysis has experienced an unprecedented growth because of their significant contributions to environmental protection and energy utilization [1–3]. Many catalytic materials have also been prepared on the nanoscale by various synthesis methods and extensively studied to fully understand their complex surface reaction processes. Ceria (CeO_2), famous for its excellent oxygen transport capacity, has been well used in industry as the main carrier of three-way catalysts (TWCs). In addition, CeO_2 performs many important functions on the nanoscale. Metal oxides, as active components on CeO_2 supports, show better reactivity and stability in catalytic processes, benefitting from oxygen transfer and other interactions between CeO_2 support and active components. CeO_2 can also keep metal oxides well dispersed and protect them from sintering at high temperature [3–7]. These profound changes in the catalytic performance are mainly attributed to differences in the nanoparticles' size and morphology. Trovarelli and Llorca [3] reviewed the recent development and applications of CeO_2 nanomaterials. Growth law and influencing factors of different CeO_2 crystal faces have been reported, showing that shape (as well as size) and surface/face reconstruction of CeO_2 can be controlled at the nanoscale. Based on these parameters, catalyst activity and stability can be effectively governed in catalytic reactions. Zhang et al. [5] developed a lattice oxygen distortion method to enhanceoxygen activation

by quenching Ce–Zr oxide nanoparticles formed at extremely hightemperature, which has been applied in the oxidation of carbon monoxide (CO). Ce–Zr oxides can provide about 19 times more oxygenvacancies than traditional oxides in CO atmosphere. Based on the above factors, nanoparticles synthesized by different methods can exhibit different catalytic activities and exploring their different reactivities is of high scientific interest [8].

CO is one of the most common toxic gases and harmful to environment and human health. The elimination of CO and especially the oxidation of CO, a simple and typical reaction in heterogeneous catalysis, has attracted wide attention in recent years due to its academic value and possible applications [9–13]. Progress in nanotechnology provides a precious tool for the study of CO oxidation at the nanoscale. In particular, nano-ceria particles play an important role as support in catalytic reactions. Nobel metals supported on CeO_2 show an excellent performance as catalysts for the oxidation of CO [14–17]. For example, Chen et al. [18] loaded Pd on the specific crystal plane of CeO_2 nanoparticles and studied the electronic metal-support interactions (EMSI) in CO oxidation. They showed that interactions on well-defined interfaces improved the catalytic performance. Tanikawa and Egawa [19] found that the addition of Ba ions to palladium catalysts on different ZrO_2 or Al_2O_3-modified CeO_2 supports affected the adsorption strength of CO on the catalysts. However, noble-metal catalysts also exhibit obvious disadvantages. They are difficult to obtain and expensive, which limits their applications. Therefore, increasing research is performed on cheap and easily available alternatives. In recent years, transition-metal oxides have become popular as non-noble metal catalysts [20–26], and their CO oxidation performance has been reported to be strongly influenced by the catalysts' structure, size, and morphology [27]. Chen et al. [28] synthesized Co_3O_4-CeO_2 core–shell catalysts and proved that the synergistic effect between Co_3O_4 and CeO_2 is responsible for their enhanced catalytic activity compared with that of regular catalysts. Narayana et al. [29] prepared spherical CeO_2 nanoparticles with Mn-ion substitution and observed the highest CO oxidation rate for the structure with the highest amounts of Mn^{2+} as well as oxygen vacancies. Obviously, nanoscale catalysts exhibit excellent catalytic performances due to the size effect and their special morphology. In addition, among noble-metal or transition-metal oxide catalysts, CeO_2 has a prominent role as one of the most widely used supports in catalytic oxidation technology.

Based on the above analysis, it can be inferred that different synthesis methods have great influence on the morphology and properties of CeO_2 nanoparticles, which may affect the catalytic performance. In this paper, nano-ceria with different sizes were prepared by hydrothermal and co-precipitation methods. The impregnation method was further used to load a specific amount of CoO_x onto the CeO_2 surface. The catalysts' CO oxidation performances were studied, and their physical and chemical properties were characterized by XRD, BET, Raman spectroscopy, H_2-TPR, O_2-TPD, and XPS. The results indicated that CeO_2 nanoparticles prepared by the hydrothermal method with a loading of 4wt% Co possess the best CO oxidation performance.

2. Results and Discussion

2.1. Catalytic Behavior

The catalytic performances of CeO_2 catalysts with different Co loadings synthesized by the hydrothermal method are shown in Figure 1. The mixed oxides revealed superior performances compared with pure CeO_2 catalyst, and the temperature of 100% conversion remarkably decreased after Co loading. However, the catalytic activity does not change linearly with increasing Co loading. The highest activity was observed for 4% Co/CeO_2, and the maximum CO conversion rate of 100% was obtained at 130 °C.

CO conversions of pure supports and catalysts with 4% Co loading, prepared by different methods, are shown in Figure 2. The catalytic activity of CeO_2 support prepared by the hydrothermal or co-precipitation method is higher than that of commercial CeO_2. For pure CeO_2-p, CeO_2-h, and CeO_2-c supports, CO conversion (10% efficiency) starts at 217, 232, and 244 °C, respectively. The CO conversion

of CeO_2-p and CeO_2-h reaches nearly 100% at 320 °C, while the efficiency of CeO_2-c is only 60% at this temperature. Interestingly, Co loading significantly improves the catalytic activity. For 4% Co/CeO_2-h and 4% Co/CeO_2-p catalysts, CO conversion (10% efficiency) starts at about 80 °C, and 4% Co/CeO_2-c reaches the same initial conversion rate at 174 °C. In addition, 4% Co/CeO_2-h displays the highest CO conversion rate among the three catalysts, yielding 100% CO conversion at 130 °C. In contrast, the second highest rate is detected for 4% Co/CeO_2-p and 4% Co/CeO_2-c, yielding 100% CO conversion at 150 and 210 °C, respectively. It can be inferred that Co is the main active component in the reaction, and different preparation methods exert significant influence on the catalytic performance. Different preparation methods may affect the catalysts structure, surface morphology, and grain size, which may change the catalytic performance. In addition, the performance is affected by the interaction between active components and supports. Therefore, we further explored the changes in the catalytic performance caused by different preparation methods.

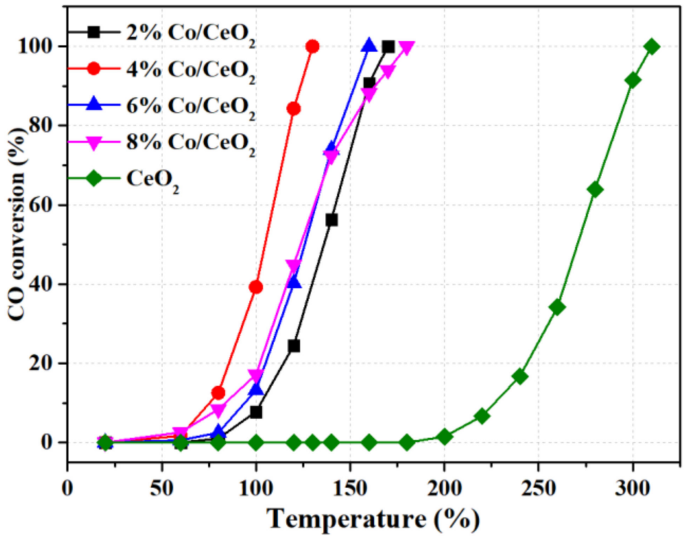

Figure 1. CO conversion as a function of Co loading for the catalysts produced by the hydrothermal method.

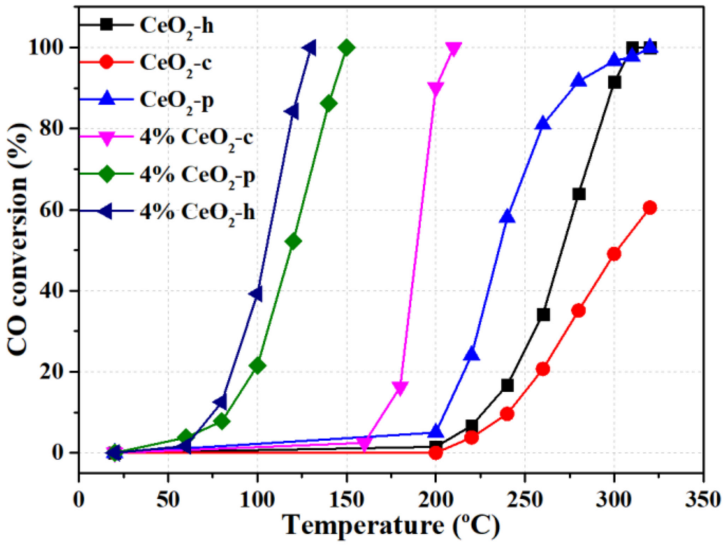

Figure 2. CO conversions of pure supports and catalysts with 4% Co loading prepared by different methods.

The activity test of CO oxidation under different gas hourly space velocities (GHSV) is presented in Figure 3. Generally, GHSV reflects the residence time of reaction gas in the catalyst bed. Higher GHSV

are correlated with shorter residence times, while lower reaction depths are correlated with larger treatment capacities. For GHSV = 12, 000 h^{-1} and GHSV = 24, 000 h^{-1}, the CO conversion rates of 4% Co/CeO_2-h are almost identical. However, when the GHSV reaches 30, 000 h^{-1}, the catalytic activity decreases slightly, but it is still larger than 90% at 136 °C. For GHSV = 48, 000 h^{-1}, the CO conversion decreases obviously, and complete CO conversion is reached at 190 °C. This temperature point is shifted back about 60 °C, and the CO conversion reaches 90% at about 166 °C. In general, when the space velocity increases to more than 24, 000 h^{-1}, the catalytic activity decreases, but complete CO conversion is still reached before 190 °C.

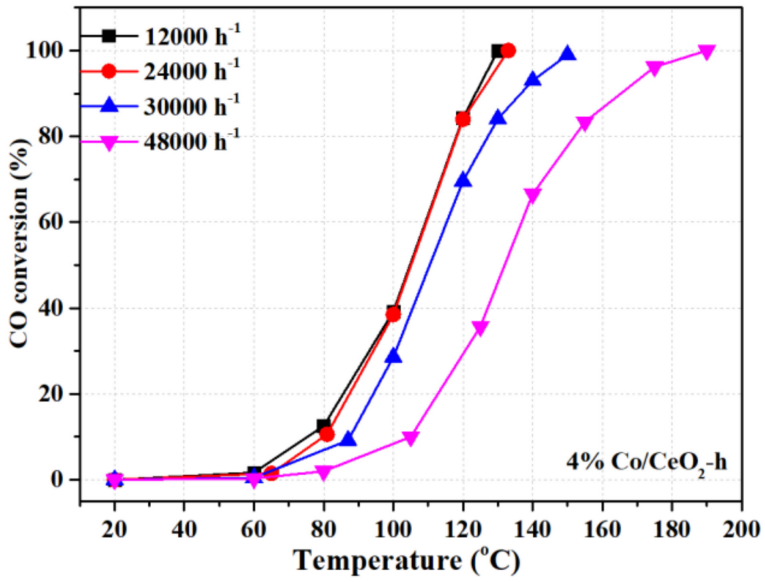

Figure 3. CO conversions of 4% Co/CeO_2-h under different gas hourly space velocity.

2.2. XRD and BET Analysis

The crystal structures of CeO_2 supports and Co/CeO_2 catalysts have been investigated by XRD, as presented in Figure 4. The XRD patterns of all pure CeO_2 samples display identical peaks, and the diffraction peaks at 28.5, 33.0, 47.5, 56.3, 59.1, 69.4, 76.8, and 79.1° could be ascribed to the (111), (200), (220), (311), (222), (400), (331), and (420) crystal planes of the face-centered cubic structure of CeO_2 (JCPD 43–1002), respectively. The CeO_2-csupport exhibits sharper diffraction peaks than CeO_2-h and CeO_2-p, which showed both very weak diffraction peaks. The intensity of the XRD diffraction peaks in the pure CeO_2 phase is related to the grain size [30]. Generally, the sharper the diffraction peak, the narrower its half-peak width and the larger the grain size. Therefore, the CeO_2 particles are smaller in CeO_2-h than those in CeO_2-c and CeO_2-p, and smaller grain size may be one of the reasons for the observed high activity of the Co/CeO_2-h catalyst [31]. Co-doping does not significantly affect the diffraction peak positions of pure CeO_2, and its original cubic fluorite structure is not obviously altered. In contrast, Co-supported catalysts exhibit diffraction peaks with higher intensity. Meanwhile, no peaks corresponding to crystalline Co oxide (CoO_x) are observed in any sample, indicating that Co is highly dispersed on the CeO_2 supports. It has been reported that high dispersion of CoO_x nanoparticles is beneficial to increase the crystallinity of CeO_2, which may be related to the strong interaction between CoO_x and CeO_2 supports. The grain size is calculated from the lowest angle diffraction peak in the XRD pattern, as shown in Table 1. This reveals that the smallest particle size is obtained for CeO_2 prepared by the hydrothermal method. In general, a smaller particle size is correlated with a higher specific surface area, which contributes to the higher dispersion of CoO_x on the surface and is beneficial to improve the catalytic activity [26,30]. This conclusion is confirmed by BET analysis.

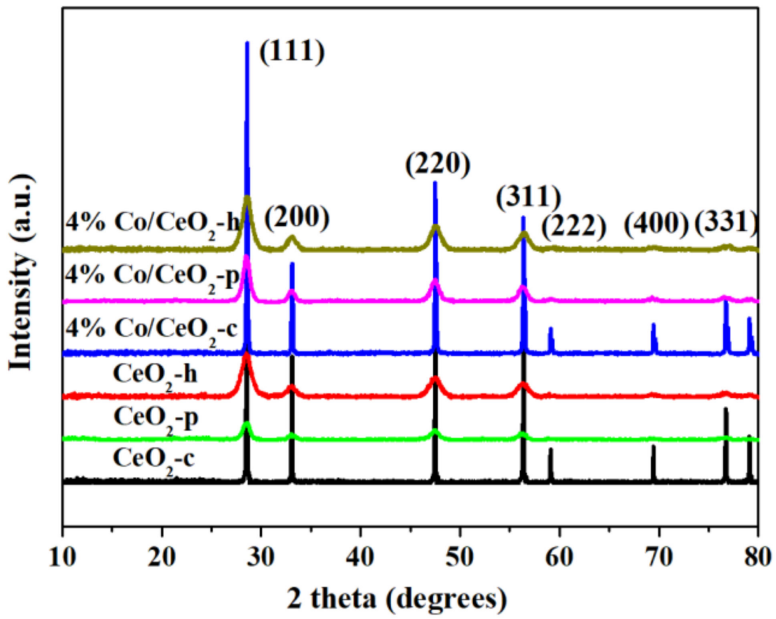

Figure 4. XRD patterns of CeO_2 supports and Co/CeO_2 catalysts.

BET surface areas of CeO_2 supports and Co/CeO_2 catalysts are listed in Table 1, revealing that CeO_2-h has a significantly higher BET surface area than CeO_2-p and CeO_2-c. For CeO_2-h and CeO_2-p, the BET surface areas decrease with increasing CoO_x loading. Interestingly, the BET surface area of 4% Co/CeO_2-c increases only slightly. However, compared with Co/CeO_2-p and Co/CeO_2-c, Co/CeO_2-h still has the highest BET surface area, and the surface area decreases in the order of Co/CeO_2-h > Co/CeO_2-p > Co/CeO_2-c. The high surface area of Co/CeO_2-h may affect the CO oxidation activity, which depends on the number of reaction sites and thus on the specific surface area.

Table 1. Physical property of the CeO_2 supports and 4% Co/CeO_2 catalysts.

Catalysts	Particle Size [a](nm)	BET Surface Area (m^2/g)	O_2 Desorption [b] (mmol/g)	H_2Consumption [c] (mmol/g)	$H/H_{theoretical}$ [d]
CeO2-h	10.0	128.1	0.82	1.19	0.59
CeO2-p	14.6	65.1	0.50	0.88	0.57
CeO2-c	>100	40.6	0	0.07	0.24
4%Co/CeO2-h	8.9	96.4	1.08	2.01	0.92
4%Co/CeO2-p	12.5	56.1	0.94	1.58	0.91
4%Co/CeO2-c	>100	43.8	0	1.11	0.74

[a] Calculated by the XRD data. [b] Calculated by O_2-TPD in the range of 20–750°C. [c] and [d] Calculated by H_2-TPR in the range of 50–600 °C.

2.3. SEM and TEM Analysis

The SEM images of 4% Co/CeO_2 catalysts are shown in Figure 5, revealing obvious differences in the particle sizes of these catalysts. The catalyst 4% Co/CeO_2-h forms regular cubes and spheres with a relatively uniform size of <400 nm diameter.The catalysts 4%Co/CeO_2-c and 4% Co/CeO_2-p form larger particles of <1.5 μm diameter. As 4% Co/CeO_2-h exhibits the smallest grain size as well as the best CO catalytic activity, a relationship between grain size and CO catalytic reactivity may be postulated. Although the grain size is not the only factor affecting the conversion efficiency, smaller grain sizes improve the CO catalytic activity. It should be noted that larger CeO_2 particles observed in SEM may also result from the agglomeration of smaller particles. However, the determination of the particle size is limited by the instrumental magnification, and TEM analysis is required to precisely determine smaller grain sizes, as described in the following.

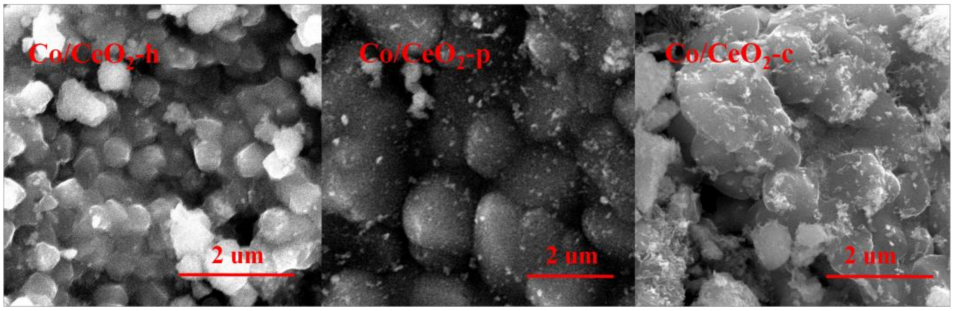

Figure 5. SEM images of 4% Co/CeO_2 catalysts.

The catalysts 4% Co/CeO_2-h, 4% Co/CeO_2-p, and 4% Co/CeO_2-c were studied by SEM-EDX elemental mapping, as shown in Figure 6. Among them, Figure 6b,e,h shows the elemental distribution of Ce, and Figure 6c,f,i shows the elemental distribution of Co of the three catalysts. The analysis reveals that the distribution of Co is more dispersed than that of Ce on Co/CeO_2-p and especially on Co/CeO_2-h. This higher dispersion of Co was theoretically expected, as Co was impregnated on the surface of CeO_2. However, the Ce and Co distributions on CeO_2-c are similar, which suggests some agglomeration of CoOx. Furthermore, the consistency of the support materials (CeO_2) indicates that CeO_2 support prepared by the hydrothermal method is more conducive to the dispersion of Co on the surface, and the Co dispersion on the support surface may be related to the interaction between Co and CeO_2 with different particle sizes and specific surface areas. EDX analysis shows, in combination with the activity test results, that the excellent Co dispersion promotes the catalytic activity.

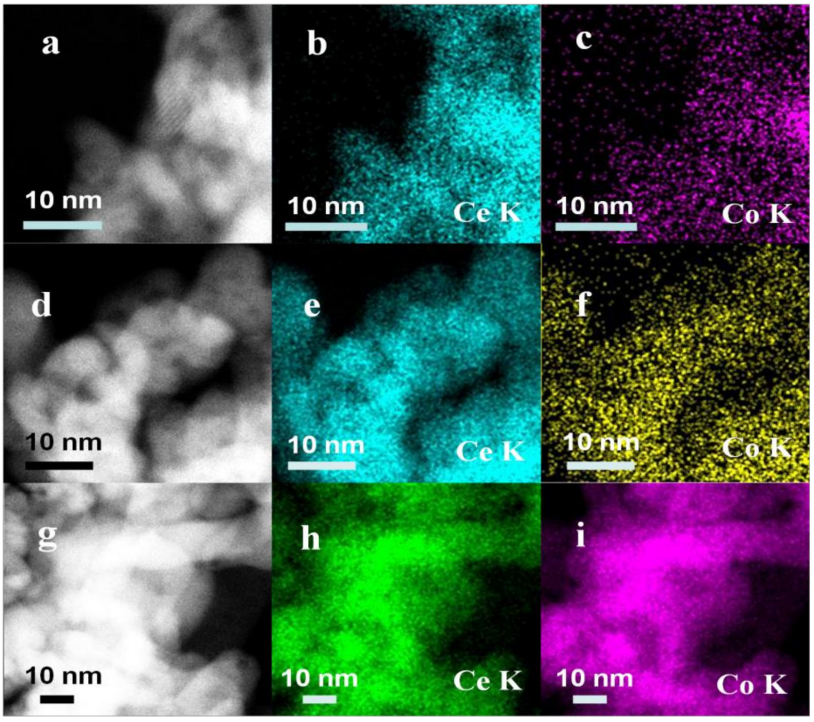

Figure 6. SEM elemental mapping for Co/CeO_2-h(**a**–**c**), Co/CeO_2-p (**d**–**f**) and Co/CeO_2-c(**g**–**i**).

TEM was performed to determine the particle sizes of Co/CeO_2-h, Co/CeO_2-p, and Co/CeO_2-c catalysts, as demonstrated in Figure 7. The images reveal the presence of CeO_2 nanoparticles in all catalysts Co/CeO_2-h (Figure 7a), Co/CeO_2-p (Figure 7d), and Co/CeO_2-c (Figure 7g). Co/CeO_2-h showed an average particle size of about 8–10 nm (Figure 7a), Co/CeO_2-p showed a larger average particle size of about 15–20 nm (Figure 7d), and Co/CeO_2-c exhibited the largest particle sizes of more than 20 nm and more regular particles than the particles of the other two catalysts (Figure 7g). These differences in

the grain sizes are consistent with previous test results. No lattice fringes corresponding to Co oxide were found, which explains, in combination with the SEM elemental mapping results, the high Co dispersion on the CeO_2 surface. Furthermore, the HRTEM images reveal lattice distances of 0.308, 0.309, and 0.311 nm for the three catalysts, which are assigned to the (111) lattice plane of CeO_2. These results fully prove the formation of CeO_2 nanoparticles.

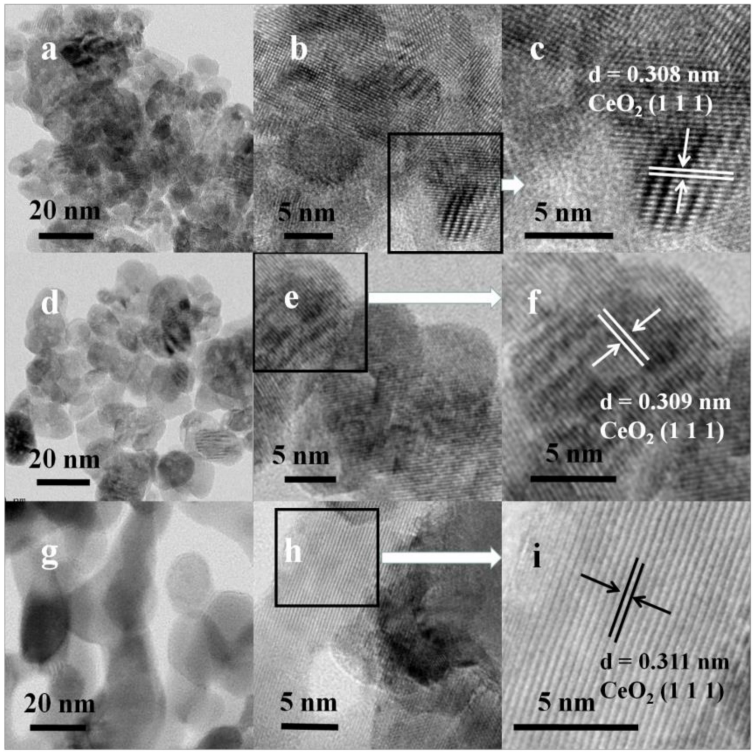

Figure 7. TEM profiles of Co/CeO_2-h(**a**–**c**), Co/CeO_2-p(**d**–**f**) and Co/CeO_2-c(**g**–**i**).

2.4. Raman Spectroscopy

The structural properties of the catalysts are very important for the analysis of active sites in solid–gas reactions. Raman spectroscopy, as a structural characterization technique, has been widely used for this purpose in different catalytic reaction systems [32–35]. The Raman spectra of all CeO_2 and Co/CeO_2 catalysts are shown in Figure 8. The distinct F_{2g} symmetry mode of the CeO_2 phase centered between 428 and 454 cm^{-1}. Two weak bands around 1158 cm^{-1} are due to the defect-induced (D) mode and the second-order longitudinal (2LO) mode [36]. CeO_2-h exhibits a much broader F_{2g} peak than CeO_2-c and CeO_2-p, which is a size-dependent phenomenon observed for ceria nanoparticles and can be explained by inhomogeneous strain broadening associated with particle size dispersion and phonon confinement [36–38]. This is consistent with XRD measurements, which revealed for CeO_2-h the smallest average particle size among all catalysts. Furthermore, the D/F_{2g} peak area ratio can be estimated to gain insight into the relative population of oxygen vacancies, as shown in the Table 2. Compared with CeO_2-c and CeO_2-p, Co/CeO_2-h reveals more oxygen vacancies. Therefore, application of high temperature and high pressure in the hydrothermal process promote the formation of oxygen vacancies, which could improve the catalytic performance.

The Raman spectra of 4% Co/CeO_2 are similar to those of the CeO_2 supports. No peaks corresponding to crystalline CoO_x were detected, which further indicates that CoO_x is highly dispersed on the support surface. The decrease of the peak intensity may be caused by the change of the relative Ce-O content. Meanwhile, Raman spectra of CeO_2 support and Co/CeO_2 catalysts prepared by different synthetic methods exhibit obvious peak shifts. The loading with cobalt oxide species slightly red-shifts the F_{2g} characteristic peaks of Co/CeO_2-p and Co/CeO_2-c. This phenomenon is usually related to the

change in lattice spacing and bond length caused by lattice constriction upon Co^{2+}-doping [37,38], as it is possible that Co ions enter the interior of the CeO_2 lattice. In contrast, the Co/CeO_2-h catalyst shows a blue shift of the F_{2g} characteristic peak. This further suggests a special interaction between CoO_x and CeO_2-h supports. CoO_x is mainly dispersed on the surface of the Co/CeO_2-h catalyst and well-dispersed cobalt oxide species contribute to the high catalytic activity of the mixed metal oxide catalysts [33,36].

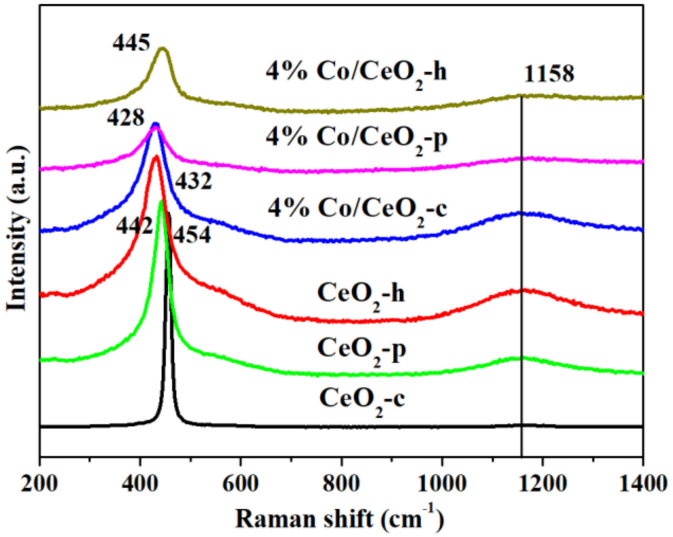

Figure 8. Raman spectra of CeO_2 supports and 4% Co/CeO_2 catalysts.

Table 2. Relative population of oxygen vacancies.

	CeO_2-c	CeO_2-p	CeO_2-h	Co/CeO_2-c	Co/CeO_2-p	Co/CeO_2-h
D/F_{2g} (%)	77.96	82.46	97.42	74.68	78.9	80.74

2.5. H_2-TPR and O_2-TPD Analysis

Temperature-programmed reduction (H_2-TPR) analysis has been conducted to investigate the reduction behavior of CeO_2 supports and Co/CeO_2 catalysts, as shown in Figure 9. The centers of the reduction peaks of pure CeO_2 supports appear at about 200–550 °C and 800 °C, which can be assigned to the reduction of surface oxygen and lattice oxygen, respectively [39]. For CeO_2-h, the centers of the reduction peaks appear at 325, 510, and 780 °C, while CeO_2-p exhibits the centers of its reduction peaks at 426, 520, and 780 °C. However, CeO_2-c shows only one reduction peak at 824 °C. These results indicate that more oxygen is adsorbed on the surfaces of CeO_2-h and CeO_2-p, which improves the catalytic activity. In addition, the initial reduction temperature of CeO_2-h at about 225 °C is lower than that of the other two supports, and the reduction peak area is larger. It can be inferred that the low temperature reduction performance of CeO_2-h is better than those of the other two catalysts. Compared with pure CeO_2 supports, the reduction peak of the Co/CeO_2 catalysts is shifted to low temperature. This indicates that Co-doping improves the redox capacity. Moreover, for Co/CeO_2 catalysts, the reduction peaks α appear between 200 and 300 °C and are mainly related to the reduction of the Co_3O_4 phase, as this Co-species is easier to reduce than Ce^{4+}. Similarly, all the samples display β peaks at about 800 °C due to the reduction of bulk CeO_2, and it can be observed that the temperature of the reduction peak decreases gradually in the order 4%Co/CeO_2-h< 4%Co/CeO_2-p < 4%Co/CeO_2-c. This further confirms that 4%Co/CeO_2-h exhibits the best reduction performance among all catalysts and that strong interactions between the active component CoO_x and CeO_2 supports are present.

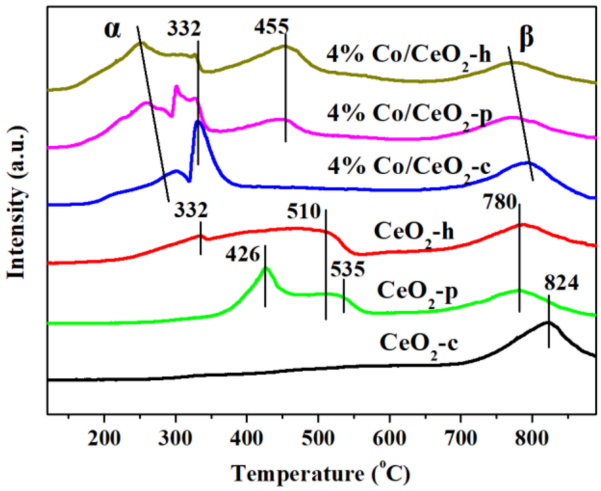

Figure 9. H_2-TPR profiles of different CeO_2 supports and 4%Co/CeO_2 catalysts.

Various studies [40–42] have shown that the reduction of Co_3O_4 is a two-step process, involving the reductions of Co_3O_4 to CoO and CoO to Co. These results clearly show that the reduction behavior of Co_3O_4 strongly depends on the CeO_2 synthesis method, dispersion state of CoO_x, and the interaction between CoO_x and CeO_2, which is consistent with conclusions of previous reports [26,43]. For the Co/CeO_2 catalysts, the reduction peaks can be classified as follows: (1) Range A (<240°C): reduction of surface-adsorbed oxygen species; (2) Range B (250–310°C): reduction of Co^{3+} to Co^{2+} on the interface between Co_3O_4 and CeO_2; (3) Range C (310–350°C): reduction of independent Co_3O_4 weakly interacting with CeO_2 to form Co; (4) Range D (350–500°C): reduction of Co^{2+} to Co [41,42]. Among these catalysts, Co/CeO_2-h displayed the lowest reduction temperature, which indicates that Co/CeO_2-h exhibits the best redox performance. Position and intensity of the reduction peaks often reflect differences in the interactions between active components and supports. The Co/CeO_2-h catalysts exhibited only very small peaks compared with pure Co_3O_4, suggesting high component dispersion in these catalysts and implying that almost all present Co-species share a homogeneous interaction with the CeO_2 phase. A rather large and sharp reduction peak appears for Co^{2+} interacting with CeO_2, which may present further evidence for this homogeneous interaction. The CoO_x dispersion in different catalysts decreases in the order Co/CeO_2-h > Co/CeO_2-p > Co/CeO_2-c, which is in good agreement with the XRD results. Thus, it can be inferred that the different preparation methods significantly influence the component dispersion. Furthermore, the hydrogen consumption of all catalysts was calculated from the H_2-TPR measurement summarized in Table 1. H_2 consumption in the range of 50–600 °C was 2.01, 1.58, 1.11, 1.19, 0.88, and 0.07 mmol/g for Co/CeO_2-h, Co/CeO_2-p, Co/CeO_2-c, CeO_2-h, CeO_2-p, and CeO_2-c, respectively. The homogeneous and profound interaction provides the largest Co_3O_4–CeO_2 interface area. Therefore, the Co/CeO_2-h catalyst is expected to contain the largest amount of adsorbed surface oxygen, as indicated by the largest H_2 consumption, resulting in an enhanced CO catalytic activity.

Since oxygen vacancies play a crucial role in CO oxidation over Co/CeO_2 catalysts, O_2-TPD measurements have been performed, as presented in Figure 10. One oxygen desorption peak at nearly 450 °C can be observed for the CeO_2-h and CeO_2-p supports, while CeO_2-c only exhibits a very small peak around 800 °C. This proves that CeO_2-h and CeO_2-p supports possess better redox performance. Furthermore, Co/CeO_2 catalysts show more chemically adsorbed oxygen species and lower desorption temperatures than pure CeO_2 supports. Except for Co/CeO_2-c, two oxygen desorption peaks can be observed for the Co/CeO_2 catalysts, while Co/CeO_2-c shows only one peak near 750°C. For Co/CeO_2-p and Co/CeO_2-h, the other wide peak α appears in the range of 150 to 680 °C. Generally, the peak β centered below 750 °C can be attributed to the oxygen desorption from Co and CeO_2 sites, and the high-temperature peak at T > 750 °C corresponds to the thermal decomposition of Co_3O_4, which is consistent with previous reports [44–46]. The peak at T < 750 °C corresponds to the amount of oxygen desorption that has been listed in Table 1. The change rule of the oxygen desorption is

consistent with activity test and H_2-TPR results. It can be seen that the 4% Co/CeO_2-h catalyst desorbs the largest amount of chemically adsorbed oxygen, indicating that this catalyst exhibits the largest oxygen amount on its surface among all catalysts, which explains its high catalytic activity. In addition, according to the literature, good performance for adsorption and activation of oxygen on the catalyst surface contributes significantly to the catalysts' activity for CO oxidation [47–49]. This is one of the most important reasons that the Co/CeO_2-h catalyst has the best CO catalytic oxidation performance. In conclusion, also these results confirmed that different synthetic methods have a significant effect on the amount of active oxygen on the catalyst surface.

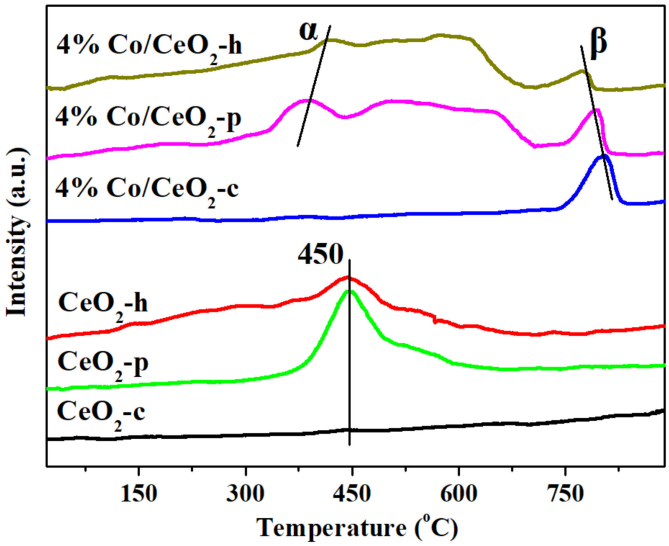

Figure 10. O_2-TPD profiles of CeO_2 supports and 4% Co/CeO_2 catalysts.

2.6. XPS Analysis

XPS analysis was carried out to study the valence states of the surface elements on different catalysts. The recorded spectra are shown in Figure 11, and the relative concentrations of the surface atoms Ce and Co are shown in Table 2, revealing that curve shape and positions are typical for Ce 3d and Co 2p. The sub-bands labeled u′ and v′ represent the $3d^{10}4f^1$ state, corresponding to Ce^{3+} cations, whereas u, u″, u‴, v, v″, and v‴ represent the $3d^{10}4f^0$ state of Ce^{4+} cations, as shown in Figure 11A [50,51]. Meanwhile, the main peaks (with satellite peaks) are detected at 775–790 eV and correspond to the binding energy of Co $2p_{3/2}$. The Co $2p_{3/2}$ spectra of the catalysts could be fitted to two peaks with satellite peaks. Binding energies of 780.5 ± 0.6 and 779 ± 0.6 eV are assigned to Co^{2+} and Co^{3+} species, respectively, as shown in Figure 11B [52]. The relative concentrations of surface atoms on the catalysts prepared by three different methods are discrepant. For Co/CeO_2-h, Co/CeO_2-p, and Co/CeO_2-c, the atomic ratios of Ce^{3+}/Ce are 16.58%, 13.50%, and 11.89%, respectively, and the atomic ratios of Co^{3+}/Co are 52.84%, 48.53%, and 45.72%, respectively shown in Table 3. It can be seen that Ce^{3+}/Ce and Co^{3+}/Co have the highest atomic ratios on the surface of Co/CeO_2-h, which also shows the best CO conversion among all tested catalysts according to the activity test results. According to the literature [53,54], the presence of Ce^{3+} may result in a charge imbalance, which leads to oxygen vacancies and unsaturated chemical bonds. This situation will generate additional chemisorbed oxygen or weakly adsorbed oxygen species on the catalyst surface. Meanwhile, the presence of Co^{3+} also enhances the redox properties of Co-based catalysts [55], as more active sites are provided by a larger amount of exposed Ce^{3+} and Co^{3+} on the catalyst surface. The Co/CeO_2-h catalyst promotes the transformations of Ce^{4+} to Ce^{3+} and Co^{2+} to Co^{3+}. Moreover, based on the charge balance, the presence of Ce^{3+} and Co^{3+} can enable the redox cycle $Ce^{4+} + Co^{2+} \leftrightarrow Ce^{3+} + Co^{3+}$, with Ce^{4+} and Co^{2+} being formed in the process of the catalytic reaction. The adsorption–desorption efficiency of CO

on the catalyst surface is promoted, and the electron transfer process accelerated by this redox cycle regenerates active sites, which enhances the CO conversion.

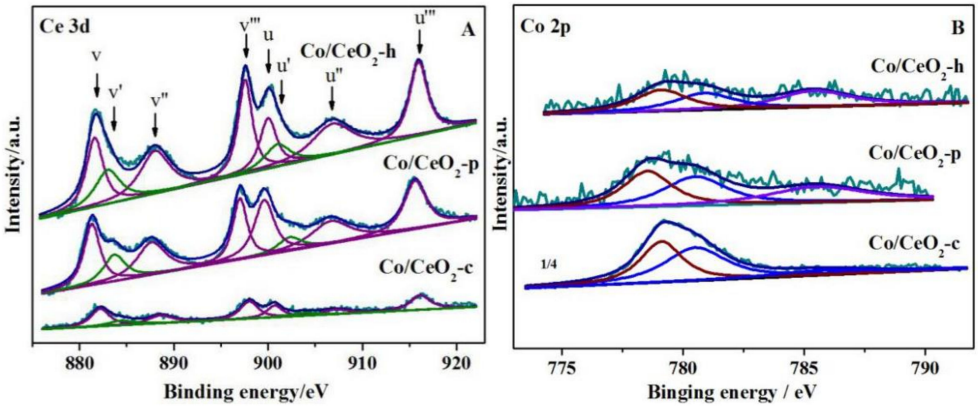

Figure 11. (**A**) Ce3d and (**B**) Co2p XPS spectrum of 4% Co/CeO_2 catalysts.

Table 3. The relative concentrations of different valence elements surface atomic Ce, Co.

Catalysts	Atomic Ratio (%)	
	Ce^{3+}/Ce	Co^{3+}/Co
4% Co/CeO_2-h	16.58	52.84
4% Co/CeO_2-p	13.50	48.53
4% Co/CeO_2-c	11.89	45.72

3. Materials and Methods

3.1. Synthesis of CeO_2 Nanoparticles

CeO_2-p was prepared by a co-precipitation method. Briefly, 10 g $Ce(NO_3)_3{\cdot}6H_2O$ was completely dissolved in 30 mL distilled water and the resulting solution was stirred adequately. Then, ammonia solution was added to the above solution to reach pH 9, and the solution was stirred for 3 h before being filtrated and washed. This sample was dried at 80 °C overnight. Finally, the obtained product was calcined in a muffle furnace at 400 °C for 4 h.

CeO_2-h was prepared by a hydrothermal method. In a typical experiment, 1 g $Ce(NO_3)_3{\cdot}6H_2O$ was dissolved in 1 mL distilled water, 1 mL ethyl acetate, and 29 mL glycol, and the resulting solution was stirred at room temperature for 10 min. Then, 2 g urea was added dropwise to the above solution under vigorous stirring. After stirring for 30 min, the mixture was transferred into a 50 mL Teflon-lined autoclave and heated at 180 °C for 4 h. The resultant solid products were collected by filtration, washed with water, dried at 80 °C, and calcined at 400 °C for 4 h under static air conditions. The obtained CeO_2 product was designated as CeO_2-h.

3.2. Synthesis of Co/CeO_2 Nanoparticles

Co/CeO_2 was synthesized by a wet impregnation method. Therefore, 0.5 g CeO_2 synthesized by the hydrothermal method was dispersed in 50 mL of the appropriate amount of $Co(NO_3)_2{\cdot}6H_2O$. The amount of $Co(NO_3)_2{\cdot}6H_2O$ was calculated to provide an amount of Co corresponding to 4wt% CeO_2. The obtained mixture was stirred at room temperature for 3 h, and excess water was evaporated completely. The product was further dried at 80 °C for 12 h and then calcined in air at 400 °C for 3 h. The resulting sample was named 4wt% Co/CeO_2-h. To study the effect of different Co loadings during CO oxidation, 2, 6, and 8wt% Co/CeO_2, commercial CeO_2 with 4%Co loading (named 4wt% Co/CeO_2-c), and CeO_2 synthesized by the co-precipitation method with 4%Co loading (named 4wt% Co/CeO_2-p) were also prepared by a similar process.

3.3. Measurement of CO Oxidation Activity

As-prepared Co/CeO_2 catalyst (100 mg; 40–60 mesh) was placed into a fixed-bed quartz tubular micro-reactor (diameter φ = 4 mm). The CO oxidation reaction was performed under a total gas flow rate of 20 mL min^{-1} (gas flow rates of 40, 50, and 80 mL min^{-1} were used to adjust the hourly space velocity of the gas). The typical reactant gas composition contains 1% CO and 5% O_2 in 99% Ar. The temperature ramp was set at 10 °C min^{-1}. The catalytic activity was examined from the decrease in the characteristic m/z 28 signal corrected for the CO_2 cracking pattern in the temperature range of 100–300 °C.

3.4. Characterization of Materials

XRD patterns were recorded on a Rigaku D/MAX-3B Auto X-ray diffractometer(Herbin, CHN, China) with Cu Kα radiation (λ = 1.5416 Å, 40 kV, 200 mA). The diffraction patterns were taken in the 2θ range of 10–80° at a scan speed of 10° min^{-1}. The Brunauer–Emmett–Teller (BET) specific surface area and the corresponding Barrett–Joyner–Halenda (BJH) pore-size distribution were measured on a micrometrics ASAP 2010M instrument(Herbin, CHN, China). Raman spectra were measured on the Raman spectrophotometer JY-HR800 operating at 458 nm(Herbin, CHN, China). H_2-TPR and O_2-TPD were measured on a multipurpose analytical system (TP-5080, company of Tianjin Xianquan). For H_2-TPR, 0.2 g of the sample was first heated to 250 °C and kept in He at 30 mL min^{-1} for 60 min. After cooling to room temperature, the sample was again heated to 800 °C at a rate of 10 °C min^{-1} under 5 vol% H_2/N_2. For O_2-TPD, 0.2 g of the sample was first heated to 250°C and kept in He at 30 mL min^{-1} for 60 min. After cooling to room temperature, the sample was exposed to pure oxygen for 60 min to achieve sufficient oxygen absorption. Then, the sample was heated to 800 °C at a heating rate of 10 °C min^{-1} under pure He at a flow rate of 30 mL min^{-1}. X-ray photoelectron spectra (XPS) were recorded on a Physical Electronics Kratos Amicus spectrometer (Herbin, CHN, China)with Al Ka radiation source. All binding energies were referenced to the C1s line at 284.8 eV. Transmission electron microscopy (TEM) measurements were taken on a JEM-2100 electron microscope operating at 200 kV(ChangChun, CHN, China). EDX elemental mapping images were recorded on a FeiNa phenom prox electron microscope operating.

4. Conclusions

The 4wt% Co/CeO_2 catalyst containing CeO_2 support synthesized by the hydrothermal method yielded nearly 100% CO conversion at 130 °C. Furthermore, CeO_2-h showed the best redox performance resulting from higher amounts of exposed Ce^{3+} (caused by oxygen vacancies) and Co^{3+} active sites (provided by highly dispersed CoOx on the support surface), which are present on the catalyst surface. In addition, a strong interaction between Co and CeO_2 supports enhances the formation of chemically adsorbed oxygen and promotes the redox cycle: $Ce^{4+} + Co^{2+} \leftrightarrow Ce^{3+} + Co^{3+}$. This redox cycle is charge balanced and further accelerates the electron transfer between CO and the active sites. Thus, the CO oxidation reaction is promoted, which may be the main reason for the excellent catalytic activity of the 4% Co/CeO_2-h catalyst.

Author Contributions: C.S. designed and performed the experiments; L.X. and X.C. analyzed the data; Y.W., Q.Z. and M.L. contributed reagents/analysis tools; C.S. finally wrote the paper. All authors have read and agreed to the published version of the manuscript.

Funding: This research was funded by Scientific Research Fund of Heilongjiang Education Department (No. 1353ZD002), scientific research projects of MudanjiangNormal University (No.GP2019002), Mu Danjiang Normal University Teaching reform project (No.19-XJ21008), the Scientific Research Fund of Heilongjiang Education Department (No. 1353MSYQN003), University Nursing Program for Young Scholars with Creative Talents in Heilongjiang Province (No. UNPYSCT-2016108).

Conflicts of Interest: The authors declare no conflict of interest.

References

1. Guan-Hung, L.; Lak, J.H.; Tsai, D.-H. Hydrogen Production via Low-Temperature Steam–Methane Reforming Using Ni–CeO_2–Al_2O_3 Hybrid Nanoparticle Clusters as Catalysts. *ACS Appl. Energy Mater.* **2019**, *2*, 7963–7971.
2. Bruix, A.; Neyman, K. Modeling Ceria-Based nanomaterials for catalysis and related applications. *Catal. Lett.* **2016**, *146*, 2053–2080. [CrossRef]
3. Alessandro, T.; Jordi, L. Ceria Catalysts at Nanoscale: How Do Crystal Shapes Shape Catalysis? *ACSCatal.* **2017**, *7*, 4716–4735.
4. Divins, N.J.; Angurell, I.; Escudero, C.; Dieste, V.; Liorca, J. Nanomaterials Influence of the support on surface rearrangements of bimetallic nanoparticles in real catalysts. *Science* **2014**, *346*, 620–623. [CrossRef]
5. Zhe, Z.; Jiafeng, Y.; Jixin, Z.; Qingjie, G.; Hengyong, X.; Felix, D.; Roland, D.; Jian, S. Tailored metastable Ce–Zr oxides with highly distorted lattice oxygen for accelerating redox cycles. *Chem. Sci.* **2018**, *9*, 3386–3394.
6. Dvořák, F.; Farnesi, C.M.; Tovt, A.; Tran, N.D.; Negreiros, F.R.; Vorokhta, M. Creating single-atom Pt-ceria catalysts by surface step decoration. *Nat. Commun.* **2016**, *7*, 10801. [CrossRef]
7. Jones, J.; Xiong, H.; Delariva, A.; Peterson, E.; Pham, H.; Challa, S.; Qi, G.; Oh, S.; Wiebenga, M.; Hernandez, X.; et al. Thermally stable single-atom platinum-on-ceriacatalysts via atomtrapping. *Science* **2016**, *353*, 150–154. [CrossRef]
8. Devaiah, D.; Reddy, L.; Park, S.; Reddy, B. Ceria-zirconia mixed oxides: Synthetic methods and applications. *Catal. Rev.* **2018**, *60*, 177–277. [CrossRef]
9. Lykaki, M.; Stefa, S.; Carabineiro, S.A.C.; Pandis, P.K.; Stathopoulos, V.N.; Konsolakis, M. Facet-Dependent Reactivity of Fe_2O_3/CeO_2 Nanocomposites: Effect of CeriaMorphology on CO Oxidation. *Catalysts* **2019**, *9*, 371. [CrossRef]
10. Lykaki, M.; Pachatouridou, E.; Carabineiro, S.A.C.; Iliopoulou, E.; Andriopoulou, C.; Kallithrakas-Kontos, N.; Boghosian, S.; Konsolakis, M. Ceria nanoparticles shape effffects on the structural defects and surface chemistry: Implications in CO oxidation by Cu/CeO_2 catalysts. *Appl.Catal. B* **2018**, *230*, 8–28. [CrossRef]
11. Kalasin, S.; Browne, E.P.; Arcaro, K.F.; Santore, M.M. Surfaces that Adhesively Discriminate Breast Epithelial Cell Lines and Lymphocytes in Buffffer and Human Breast Milk. *ACS Appl. Mater. Interfaces* **2019**, *11*, 17035–17049. [CrossRef] [PubMed]
12. Puigdollers, A.R.; Pacchioni, G. CO Oxidation on Au Nanoparticles Supported on ZrO_2: Role of Metal/Oxide Interface and Oxide Reducibility. *ChemCatChem* **2017**, *9*, 1119–1127. [CrossRef]
13. Shen, W.; Mao, D.; Luo, Z.; Yu, J. CO oxidation on mesoporous SBA-15 supported CuO–CeO_2 catalyst prepared by a surfactant-assisted impregnation method. *RSC Adv.* **2017**, *7*, 27689–27698. [CrossRef]
14. Junhao, L.; Zhongqi, L.; David, A.C.; Wenhui, H.; Jier, H.; Libo, Y.; Zhenmeng, P.; Peilin, L.; Ruigang, W. Distribution and Valence State of Ru Species on CeO_2 Supports: Support Shape Effect and Its Influence on CO Oxidation. *ACS Catal.* **2019**, *9*, 11088–11103.
15. Dong, G.; Wang, J.; Gao, Y.; Chen, S. A Novel Catalyst for CO Oxidation at Low Temperature. *Catal. Lett.* **1999**, *58*, 37–41. [CrossRef]
16. Spezzati, G.; Su, Y.; Hofmann, J.; Benavibez, A.; Delariva, A.; Mccabe, J.; Datye, A.; Hensen, E. Atomically dispersed Pd-O species on CeO_2(111) as highly active sites for low-temperature CO oxidation. *ACS Catal.* **2017**, *7*, 6887–6891. [CrossRef]
17. Gulyaev, R.; Slavinskaya, E.; Novopashin, S.; Smovzh, D.; Zaikovsdii, A.; Osadchii, D.; Bulavchenkoa, O.; Koreven, S.; Boronin, A. Highly active PdCeOx composite catalysts for low-temperature CO oxidation, prepared by plasma-arc synthesis. *Appl. Catal. B* **2014**, *147*, 132–143. [CrossRef]
18. Yarxin, C.; Junxiao, C.; Weiye, Q.; George, C.; Aouine, M.; Vernous, P.; Xingfu, T. Well-Defined Palladium-Ceria Interfacial Electronic Effects Trigger CO Oxidation. *Chem. Commun.* **2018**, *54*, 10140–10143.
19. Xin, J.; Yang, D.; Dapeng, L.; Xilan, F.; Wang, L.; Zheng, Z.; Yu, Z. CO Oxidation Catalyzed by Two-Dimensional Co_3O_4/CeO_2 Nanosheets. *ACS Appl. Nano Mater.* **2019**, *2*, 5769–5778.
20. Liang, J.; Yang, X.; Wang, A.; Zhang, T.; Li, J. Theoretical investigations of non-noble metal single-atom catalysis: Ni_1/FeO_x for CO oxidation. *Catal. Sci. Technol.* **2016**, *6*, 1017–1036. [CrossRef]
21. Zhou, L.; Li, X.; Yao, Z.; Chen, Z.; Hong, M.; Zhu, R.; Liang, Y.; Zhao, J. Transition-Metal Doped Ceria Microspheres with Nanoporous Structures for CO Oxidation. *Sci. Rep.* **2016**, *6*, 23900. [CrossRef] [PubMed]

22. Liu, Z.; Wu, Z.; Peng, X.; Binder, A.; Chai, S.; Dai, S. Origin of active oxygen in a ternary CuO_x/Co_3O_4-CeO_2 catalyst for CO oxidation. *J. Phys. Chem. C* **2014**, *118*, 27870–27877. [CrossRef]
23. Thomas, K.; Manos, M. Transition Metal Atoms Embedded in Graphene: How Nitrogen Doping Increases CO Oxidation Activity. *ACS Catal.* **2019**, *9*, 6864–6868.
24. Cui, L.; Di, Z.; Yang, Y.; Wang, Y.; Zhang, X. Synthesis of highly efficient α-Fe_2O_3 catalysts for CO oxidation derived from MIL-100(Fe). *J. Solid State Chem.* **2017**, *247*, 168–172. [CrossRef]
25. Kaplin, I.; Lokteva, S.; Golubina, E.; Maslakov, K.; Strokova, N.; Chernyak, S.; Lunin, V. Sawdust as an effective biotemplate for the synthesis of $Ce_{0.8}Zr_{0.2}O_2$ and CuO–$Ce_{0.8}Zr_{0.2}O_2$ catalysts for total COE oxidation. *RSC Adv.* **2017**, *7*, 51359–51372. [CrossRef]
26. Jampaiah, D.; Venkataswamy, P.; Coyle, V.E.; Reddy, B.M.; Bhargava, S.K. Low-temperature CO oxidation over manganese, cobalt, and nickel doped CeO_2 nanorods. *RSC Adv.* **2016**, *6*, 80541–80548. [CrossRef]
27. Lee, J.; An, K. Catalytic CO Oxidation on Nanocatalysts. *Top. Catal.* **2018**, *61*, 986–1001. [CrossRef]
28. Chen, G.; Xu, Q.; Wang, Y.; Song, G.; Li, C.; Zhao, W.; Fan, W. Solubility Product Difference-Guided Synthesis of Co_3O_4-CeO_2 Core-Shell Catalysts for CO Oxidation. *Catal. Sci. Technol.* **2016**, *6*, 7273–7279. [CrossRef]
29. Narayana, B.; Mukri, B.; Ghosal, P.; Subrahmanyam, C. Mn Ion substituted CeO_2 Nano spheres for Low Temperature CO Oxidation: The Promoting Effect of Mn Ions. *Chem. Sel.* **2016**, *1*, 3150–3158.
30. Gao, Y.; Wang, W.; Chang, S.; Huang, W. Morphology Effect of CeO_2 Support in the Preparatport Interaction, and Catalytic Performance of Pt/CeO_2 Catalysts. *ChemCatChem* **2013**, *5*, 3610–3620. [CrossRef]
31. Junemin, B.; Dongjae, S.; Hojin, J.; Beom-Sik, K.; Jeong Woo, H.; Hyunjoo, L. Highly Water-Resistant La-Doped Co_3O_4 Catalyst for CO Oxidation. *ACS Catal.* **2019**, *9*, 10093–10100.
32. Lei, L.; Qilei, Y.; Changyu, Z.; Jinlong, Y.; Yue, P.; Junhua, L. Hollow-Structural Ag/Co_3O_4Nanocatalyst for CO Oxidation: Interfacial Synergistic Effect. *ACS Appl. Nano Mater.* **2019**, *2*, 3480–3489. [CrossRef]
33. Rashad, M.; Rüsing, M.; Berth, G.; Lischka, K.; Pawlis, A. CuO and Co_3O_4 Nanoparticles: Synthesis, Characterizations, and Raman Spectroscopy. *J.Nanomater.* **2013**, *2013*, 714853. [CrossRef]
34. Gao, X.; Qin, X. Effect of cobalt oxide on surface structure of alumina supported molybdena catalysts studied by in situ Ramanspectroscopy. *Catal. Lett.* **1993**, *18*, 409–418. [CrossRef]
35. Singhania, A.; Gupta, S. $CeO_{2-x}N_x$ Solid Solutions: Synthesis, Characterization, Electronic Structure and Catalytic Study for CO Oxidation. *Catal. Lett.* **2018**, *148*, 2001–2007. [CrossRef]
36. Niu, G.; Hildebrandt, E.; Schubert, M.; Boscherini, F.; Zoellner, M.; Alff, L.; Walczyk, D.; Zaumseil, P.; Costina, L.; Wilkens, H.; et al. Oxygen Vacancy Induced Room Temperature Ferromagnetism in Pr-Doped CeO_2 Thin Films on Silicon. *ACS Appl. Mater. Interfaces* **2014**, *6*, 17496–17505. [CrossRef]
37. LEE, Y.; He, G.; Akey, A.J.; Si, R.; Stephanopuulos, M. Raman analysis of mode softening in nanoparticle $CeO_{(2-\delta)}$ and Au-$CeO_{(2-\delta)}$ during CO oxidation. *J. Am. Chem. Soc.* **2011**, *133*, 12952–12955. [CrossRef]
38. Parvulescu, V.; Tiseanu, C. Local structure in CeO_2 and CeO_2-ZrO_2 nanoparticles probed by Eu luminescence. *Catal. Today* **2015**, *253*, 33–39. [CrossRef]
39. Luo, J.; Meng, M.; Yao, J.; Li, J.; Zha, Y.; Wang, X.; Zhang, T. One-step synthesis of nanostructured Pd-doped mixed oxides MO_x-CeO_2 (M=Mn, Fe, Co, Ni, Cu) for efficient CO and C_3H_8 total oxidation. *Appl.Catal. B* **2009**, *87*, 92–103. [CrossRef]
40. Yafeng, C.; Jia, X.; Yun, G.; Jingyue, L. Ultrathin, Polycrystalline, Two-Dimensional Co_3O_4 for Low-Temperature CO Oxidation. *ACS Catal.* **2019**, *9*, 2558–2567.
41. Cronauer, D.; Kropf, A.; Marshall, C.; Gao, P.; Hopps, S.; Jacobs, G.; Davis, B. Fischer–Tropsch Synthesis: Preconditioning Effects Upon Co-Containing Promoted and Unpromoted Catalysts. *Catal. Lett.* **2012**, *142*, 698–713. [CrossRef]
42. Reddy, B.; Rao, K.; Bharali, P. Copper Promoted Cobalt and Nickel Catalysts Supported on Ceria−Alumina Mixed Oxide: Structural Characterization and CO Oxidation Activity. *Ind. Eng. Chem. Res.* **2009**, *48*, 8478–8486. [CrossRef]
43. Hou, X.; Wang, Y.; Zhao, Y. Effect of CeO_2 Doping on Structure and Catalytic Performance of Co_3O_4 Catalyst for Low-Temperature CO Oxidation. *Catal. Lett.* **2008**, *123*, 321–326. [CrossRef]
44. Qin, H.; Qian, X.; Tao, M.; Lin, Y.; Ma, Z. Pt/MO_x/SiO_2, Pt/MO_x/TiO_2, and Pt/MO_x/Al_2O_3 Catalysts for CO Oxidation. *Catal.* **2015**, *5*, 606–633. [CrossRef]
45. Jie, L.; Lu, G.; Wu, G.; Mao, D.; Wang, Y.; Guo, Y. Promotional role of ceria on cobaltosic oxide catalyst for low-temperature CO oxidation. *Catal. Sci. Technol.* **2012**, *2*, 1865–1871.

46. Kaidong, W.; Can, W.; Feng, W.; Nan, J.; Guoqiang, J. Co/Co_3O_4 Nanoparticles Coupled with Hollow Nanoporous Carbon Polyhedrons for the Enhanced Electrochemical Sensing of Acetaminophen. *ACS Sustain. Chem. Eng.* **2019**, *7*, 18582–18592.
47. Lou, Y.; Cao, X.; Lan, J.; Wang, L.; Dai, Q.; Guo, Y.; Ma, J.; Zhao, Z.; Guo, Y.; Hu, P.; et al. Ultralow-temperature CO oxidation on an In_2O_3-Co_3O_4catalyst: A strategy to tune CO adsorption strength and oxygen activation simultaneously. *Chem.Commun.* **2014**, *50*, 6835–6838. [CrossRef]
48. Kezhi, L.; Jianjun, C.; Yue, P.; Weichen, L.; Tao, Y.; Junhua, L. The relationship between surface open cells ofa-MnO_2 and CO oxidation ability from a surface point of view. *J. Mater. Chem. A* **2017**, *5*, 20911–20921.
49. Hyunwoo, H.; Sinmyung, Y.; Kwangjin, A.; Hyun, Y.K. Catalytic CO Oxidation over Au Nanoparticles Supported on CeO_2 Nanocrystals: Effect of the Au–CeO_2 Interface. *ACS Catal.* **2018**, *8*, 11491–11501.
50. Shan, W.; Liu, F.; He, H.; Shi, X.; Zhang, C. A superior Ce-W-Ti mixed oxide catalyst for the selective catalytic reduction of NO_x with NH_3. *Appl. Catal. B* **2012**, *115*, 100–106. [CrossRef]
51. Peng, Y.; Wang, C.; Li, J. Structure–activity relationship of VO_x/CeO_2 nanorod for NO removal with ammonia. *Appl. Catal. B* **2014**, *144*, 538–546. [CrossRef]
52. Li, J.; Lu, G.; Wu, G.; Mao, D.; Guo, Y.; Wang, Y.; Guo, Y. Effect of TiO_2 crystal structure on the catalytic performance of Co_3O_4/TiO_2 catalyst forlow-temperature CO oxidation. *Catal. Sci. Technol.* **2014**, *4*, 1268–1275. [CrossRef]
53. Chuanyi, J.; Xijun, W.; Wenhui, Z.; Zhunzhun, W.; Oleg, V.P.; Yi, L.; Jun, J. Catalytic Chemistry Predicted by a Charge Polarization Descriptor: Synergistic O_2 Activation and CO Oxidation by Au–Cu Bimetallic Clusters on TiO_2(101). *ACS Appl. Mater. Interfaces* **2019**, *11*, 9629–9640.
54. Li, H.; Wu, C.; Li, Y.; Zhang, J. Superior activity of MnO_x-CeO_2/TiO_2 catalyst for catalytic oxidation of elemental mercury at low flue gas temperatures. *Appl. Catal. B* **2012**, *111*, 381–388. [CrossRef]
55. Liu, J.; Li, X.; Zhao, Q.; Ke, J.; Xiao, H.; Lv, X.; Liu, S.; Tade, M.; Wang, S. Mwchanistic investigation of the enhanced NH_3-SCR on cobalt-decorated Ce-Ti mixed oxide: In situ FTIR analysis for structure-activity aorrelation. *Appl. Catal. B* **2017**, *300*, 297–308. [CrossRef]